Bioorganic Chemistry 178 (2026) 109949

Contents lists available at ScienceDirect

Bioorganic Chemistry

journal homepage: www.elsevier.com/locate/bioorg

In silico characterisation of a novel SARS-CoV-2 envelope protein inhibitor and *in vitro* validation against murine coronavirus

Nina Kobe [a,b,*], Lennart Dreisewerd [c,d], Miha Lukšič [c], Matic Pavlin [d], Uroš Grošelj [c], Črtomir Podlipnik [c], Mojca Janc [a,b], Živa Lengar [a], Polona Mrak [e], Magda Tušek Žnidarič [a], Maruša Pompe Novak [a,f], Urška Kuhar [g], Peter Hostnik [g], Federica Dattola [h], Tea Carletti [h], Alessandro Marcello [h], Polona Kogovšek [a]

[a] *National Institute of Biology, Department of Biotechnology and Systems Biology, Večna pot 121, SI-1000 Ljubljana, Slovenia*
[b] *Jožef Stefan International Postgraduate School, Jamova cesta 39, Ljubljana SI-1000, Slovenia*
[c] *University of Ljubljana, Faculty of Chemistry and Chemical Technology, Večna pot 113, Ljubljana SI-1000, Slovenia*
[d] *National Institute of Chemistry, Department of Catalysis and Chemical Reaction Engineering, Hajdrihova 19, Ljubljana SI-1001, Slovenia*
[e] *University of Ljubljana, Biotechnical Faculty, Department of Biology, Jamnikarjeva 101, SI-1000 Ljubljana, Slovenia*
[f] *University of Nova Gorica, School for Viticulture and Enology, Glavni trg 8, SI-5271 Vipava, Slovenia*
[g] *University of Ljubljana, Veterinary Faculty, Institute for Microbiology and Parasitology, Gerbičeva 60, SI-1000 Ljubljana, Slovenia*
[h] *International Centre for Genetic Engineering and Biotechnology, Laboratory of Molecular Virology, Padriciano 99, IT-34149 Trieste, Italy*

ARTICLE INFO

Keywords:
SARS-CoV-2 envelope protein
Viroporin
Ion channel blockers
Molecular docking
Molecular dynamics simulations
Drug discovery
Murine hepatitis virus
In vitro

ABSTRACT

The emergence of new severe acute respiratory syndrome coronavirus 2 (SARS-CoV-2) variants poses a challenge to current therapies and emphasises the need for targets that are less susceptible to mutation. The SARS-CoV-2 envelope protein (Epro) is a highly conserved viroporin and is of central importance to the viral life cycle, yet it remains underexplored as a therapeutic target. In this study, we have identified and characterised a novel lead candidate (LC) – (*S*)-*N*-(2-((1*S*,3*S*,5*S*,7*S*)-adamantan-2-yl)ethyl)-2-(butylamino)-3-(1*H*-indol-3-yl)propanamide – for inhibition of the SARS-CoV-2 Epro ion channel using combined *in silico* and *in vitro* approaches. Molecular dynamics (MD) simulations showed that LC forms stable complexes at the N-terminal vestibule, with key interactions at GLU8, THR9, THR11, ASN15, and LEU18, and a calculated binding affinity higher than that of the reference compound rimantadine within the applied MD/molecular mechanics Poisson–Boltzmann surface area (MM-PBSA) framework. Results of *in vitro* experiments indicated that LC inhibits the model coronavirus murine hepatitis virus at late stages of the viral cycle. Activity under co-treatment conditions further suggests a direct virucidal effect or interference with early entry stages; an EC_{50} of approximately 12 μM was within the same micromolar range as those observed for the reference Epro inhibitors 5-(*N*,*N*-hexamethylene)amiloride and rimantadine. Quantitative PCR experiments showed delayed RNA replication in LC-treated infected cells, while light and transmission electron microscopy displayed the reduced release of virions and prevention of cell lysis. These results emphasise the central role of the Epro ion channel in the coronavirus life cycle and present LC as a promising candidate for the further development of novel coronavirus inhibitors.

Abbreviations: AMT, Amantadine; ATCC, American type culture collection; CC_{50}, Half-maximal cytotoxic concentration; CCK-8, Cell counting Kit-8; CoV, Coronavirus; COVID-19, Coronavirus disease 2019; CTD, C-terminal domain; EC_{50}, Half-maximal effective concentration; Epro, Envelope protein; ER, Endoplasmic reticulum; ERGIC, ER–Golgi intermediate compartment; FKKTLib, FKKT compound library; GAPDH, Glyceraldehyde-3-phosphate dehydrogenase; HIV-1, Human immunodeficiency virus type 1; HMA, 5-(*N*,*N*-hexamethylene)amiloride; IAV, Influenza A virus; LC, Lead candidate; MD, Molecular dynamics; MHV, Murine hepatitis virus; MM-PBSA, Molecular mechanics Poisson–Boltzmann surface area; MOI, Multiplicity of infection; M2, Matrix protein 2; NTD, N-terminal domain; POPC, 1-palmitoyl-2-oleoylphosphatidylcholine; RMSD, Root mean square deviation; RMT, Rimantadine; SARS-CoV-1, Severe acute respiratory syndrome coronavirus 1; SARS-CoV-2, Severe acute respiratory syndrome coronavirus 2; SD, Standard deviation; SI, Selectivity index; SPR, Surface plasmon resonance; TEM, Transmission electron microscopy; TMD, Transmembrane domain; ToA, Time-of-addition; VpU, Viral protein U..

* Corresponding author at: National Institute of Biology, Department of Biotechnology and Systems Biology, Večna pot 121, SI-1000 Ljubljana, Slovenia.
E-mail address: nina.kobe@nib.si (N. Kobe).

https://doi.org/10.1016/j.bioorg.2026.109949
Received 26 December 2025; Received in revised form 14 April 2026; Accepted 4 May 2026
Available online 6 May 2026

1. Introduction

The global outbreak of coronavirus disease 2019 (COVID-19), caused by severe acute respiratory syndrome coronavirus 2 (SARS-CoV-2), was the most recent pandemic. In response, significant progress has been made in understanding the pathogenesis of the virus, leading to the development of second- and third-generation vaccines and targeted small-molecule antivirals. These measures were initially effective in both the prevention and treatment of COVID-19. However, the emergence of new variants, especially Omicron, which is characterised by numerous mutations, compromised vaccine-induced immunity [1]. Several clinically approved antivirals are available for treating COVID-19; yet their clinical utility is restricted by safety, efficacy, and resistance concerns [2–5].

The genome of SARS-CoV-2 encodes four main structural proteins: spike (S), nucleocapsid (N), membrane (M), and envelope (E) protein (Fig. 1A) [6]. Despite being the smallest with only 75 amino acids, Epro plays a crucial role in the viral life cycle and is remarkably well conserved in all variants [7]. Comparative analyses show that the envelope protein (Epro) has the lowest mutation rate among the structural proteins and shows a high degree of sequence conservation between severe acute respiratory syndrome coronavirus 1 (SARS-CoV-1) and SARS-CoV-2 [7–10]. Structurally, it consists of three different domains: a short hydrophilic N-terminal domain (NTD), a central hydrophobic transmembrane domain (TMD), and a longer hydrophilic C-terminal domain (CTD) [6]. Intracellularly, Epro is predominantly localised in the endoplasmic reticulum (ER), the Golgi apparatus, and the ER-Golgi intermediate compartment (ERGIC) (Fig. 1C). These organelles are essential for the assembly, maturation, and release of newly formed virions – processes in which Epro has been shown to play a crucial role [11–14]. Recombinant coronaviruses (CoVs) lacking Epro have lower viral titres and produce incompetent progeny, indicating the functional importance of Epro for CoV pathogenesis, despite it not being strictly essential for viral replication [12,15,16].

Epro monomers oligomerise into homopentameric ion channels (so-called viroporins), which are cation-selective and cause ionic imbalances, disrupting pH gradients in host cells (Fig. 1B) [17–19]. Epro can act as an independent virulence factor, inducing apoptosis and triggering cytokine storms, thereby exacerbating disease progression [12,20]. The functional significance of viral ion channels as antiviral targets is well documented for several RNA viruses, such as influenza A virus (IAV) and human immunodeficiency virus-1 (HIV-1), which express matrix protein 2 (M2) and viral protein U (VpU) ion channels, respectively. Herein, M2 and VpU ion channel activities are closely linked to key phases of the viral life cycle, as demonstrated by mutational studies and channel-blocking compounds [21–24]. Similar findings have been obtained for CoV Epro, where inhibition of its viroporin activity has proven to be a promising antiviral strategy. Several small-molecule inhibitors – including 5-(*N*,*N*-hexamethylene)amiloride (HMA) [25–28], amantadine (AMT) [7,29,30], and rimantadine (RMT) [7,30,31] – have been characterised using techniques such as surface plasmon resonance (SPR), antiviral efficacy assays [32], and patch-clamp electrophysiology [31], demonstrating their ability to bind to the channel pore and block cation conduction. However, most Epro inhibitor candidates have so far only been identified through *in silico* studies [6,33,34], and relatively few have been validated *in vitro* or *in vivo*, highlighting the importance of experimental exploration.

In this comprehensive study, we report the identification of a novel inhibitor ((*S*)-*N*-(2-((1*S*,3*S*,5*S*,7*S*)-adamantan-2-yl)ethyl)-2-(butylamino)-3-(1*H*-indol-3-yl)propanamide) of SARS-CoV-2 Epro by combining computational and experimental approaches. Classical molecular dynamics (MD) simulations revealed that our lead candidate binds with high affinity to the N-terminal vestibule of the SARS-CoV-2 Epro ion channel. Its antiviral activity was confirmed *in vitro* against murine hepatitis virus (MHV), a model betacoronavirus (β-CoV), in L929 fibroblasts. MHV, SARS-CoV-2, and other CoVs have similar structures that overlap in several domains and show overall structural homology [35–38]. Plaque reduction assays showed a concentration-dependent decrease in viral infectivity at micromolar concentrations, comparable to known Epro inhibitors (Fig. 2). Quantitative PCR analyses indicated that LC does not directly inhibit viral genome replication but instead delays it, while light and transmission electron microscopy showed that LC interferes with viral egress after replication, thereby limiting the spread of infection to neighbouring cells. These observations suggest a multifaceted antiviral mechanism of LC that warrants further investigation.

2. Materials and methods

2.1. Candidate sourcing, molecular docking, and molecular dynamics simulations

The candidate was obtained from the FKKT Compound Library (FKKTLib; Faculty of Chemistry and Chemical Technology, University of

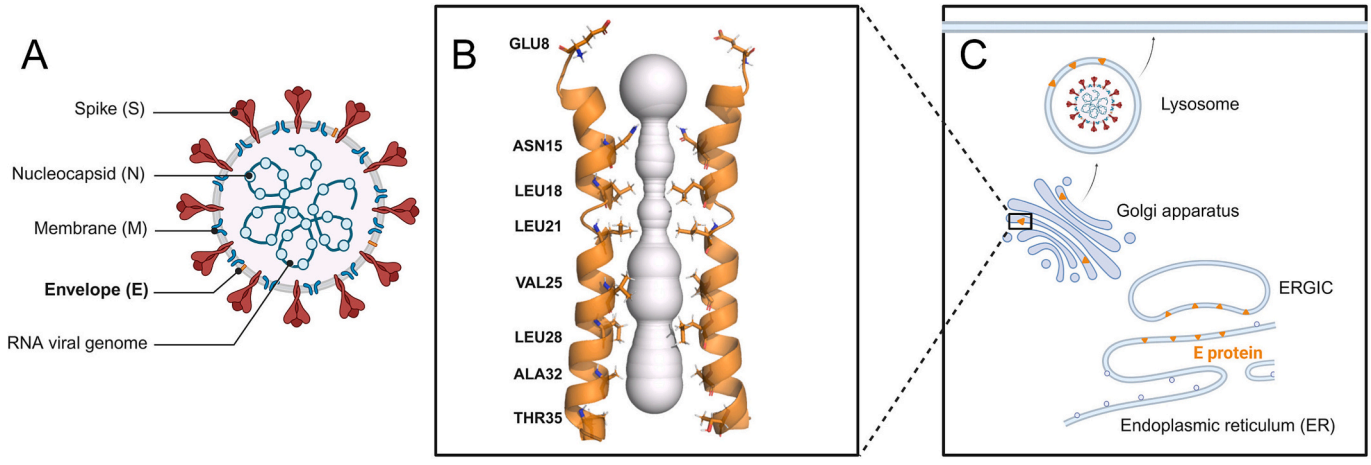

Fig. 1. **(A)** Four structural proteins of SARS-CoV-2 include spike (S), membrane (M), nucleocapsid (N), and envelope protein (E). **(B)** Cross-sectional view of SARS-CoV-2 Epro showing the Caver 3.0-calculated volume of the ion channel (grey), which extends along the longitudinal axis of the five SARS-CoV-2 Epro subunits (orange), with the channel-facing amino acid residues listed on the left. **(C)** Intracellular localisation of Epro viroporins in the endoplasmic reticulum (ER), ER-Golgi intermediate compartment (ERGIC), Golgi apparatus, and lysosomes (marked with orange).

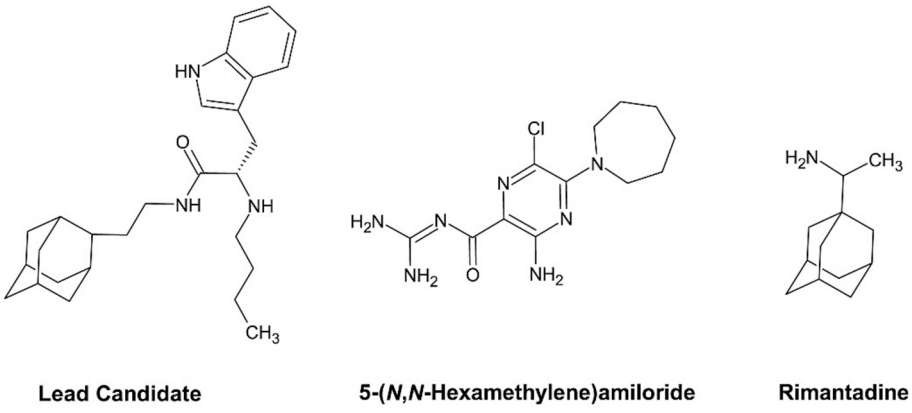

Fig. 2. Chemical structures of the tested compounds.

Ljubljana), which contains 3428 unique, literature-documented synthetic compounds. The FKKTLib was searched for adamantane substructures to identify scaffold-bearing candidates.

Molecular docking, molecular dynamics simulations, and molecular mechanics Poisson–Boltzmann surface area (MM-PBSA) analyses were performed as described previously [34]; a full description of the protocol is provided in the Supplementary material (S1). We note that MM-PBSA results should be interpreted comparatively rather than absolutely, as the method is intended as a cost-effective approach for ranking a series of related organic ligands that bind to the same protein. Protonation states for key titratable residues with previously established assignments [18] (*e.g.* GLU8) were set accordingly, while all remaining sites were set to their expected states at physiological pH. Although alternative charge states or dynamic protonation could influence local interactions, we applied a single fixed protonation scheme across all simulations to maintain consistency and avoid introducing uncertainty into the comparative analysis.

2.2. Cell line and virus

L929 mouse fibroblast cells (number CCL-1) were purchased from the American Type Culture Collection (ATCC) and cultured in complete Eagle's Minimum Essential Medium (EMEM, ATCC, USA), supplemented with 10% horse serum (HS, ThermoFisher, Paisley, UK) and 10,000 units/mL of penicillin and 10,000 µg/mL of streptomycin (ThermoFisher, Paisley, UK), in a 5% CO_2 atmosphere at 37 °C. Murine hepatitis virus strain A59 (MHV-A59) was purchased from ATCC (VR-764) and propagated in L929 cells. Viral titre was determined by 50% tissue culture infective dose ($TCID_{50}$) according to the cytopathic effect by use of the Reed–Muench method [39]. All experiments were performed in a biosafety level 2 (BSL-2) laboratory.

2.3. Compounds

The lead candidate (LC) was synthesised as reported by Meden et al. [40]. 5-(*N*,*N*-hexamethylene)amiloride (HMA) and rimantadine hydrochloride (RMT) were purchased from Sigma-Aldrich (USA). The structures are shown in Fig. 2. LC and HMA were dissolved in DMSO, and RMT was dissolved in water and stored at −20 °C until use.

2.4. Cytotoxicity assay

The cell counting kit-8 (CCK-8, Abcam) test was performed according to the manufacturer's protocol. Cells were seeded at a density of 3×10^5 cells/mL in 96-well plates and treated with different concentrations of the compounds after 24 h at 37 °C. In all experiments, a solvent control (growth medium containing 0.5% DMSO), a negative control (growth medium), and assay-specific positive controls were included. After 48 h at 37 °C, 10 µL of CCK-8 reagent was added to each well, and the cells were incubated in the dark at 37 °C for 1.5 h. The absorbance was measured at 460 nm using the Cytation 5 (Agilent BioTek). Relative cell viability was determined using the following formula: Cell viability (%) = OD of the sample / average OD of the negative control × 100%. Each compound was tested in three independent biological replicates ($N = 3$), with five technical replicates ($n = 5$) per condition in each biological replicate.

2.5. Time of addition assay and plaque reduction assay

L929 cells at a density of 3×10^5 cells/mL were seeded in 12-well culture plates and incubated at 37 °C for 24 h. Dilutions of the compounds were added 2 h before infection (pre-treatment), simultaneously with the virus after 1 h co-incubation of virus and compound at room temperature (co-treatment), or 1 h after infection (post-treatment) (Fig. 3). The cell culture supernatants collected after 48 h were used to determine the number of plaques by plaque reduction assay experiments. Experiments were performed in three independent biological replicates ($N = 3$), with two technical replicates per condition in each experiment ($n = 2$). The extended protocol is available in the Supplementary material (S2–1 and S2–2), and raw data is available at Zenodo [41].

2.6. Real-time quantitative polymerase chain reaction

L929 cells were seeded in 12-well culture plates and, after 24 h, inoculated with MHV at a multiplicity of infection (MOI) of 0.001 for 1 h at 37 °C and 5% CO_2. The inoculum was replaced with complete EMEM containing either the highest non-toxic concentration of the inhibitor (LC, HMA, or RMT) or, for infected untreated controls, the corresponding vehicle alone (0.5% DMSO). All experiments were performed under post-treatment conditions. Negative control samples were neither infected nor treated. Experiments were performed in two biological replicates ($N = 2$) for HMA and RMT, and three biological replicates ($N = 3$) for LC, with three technical replicates per condition ($n = 3$). The presence and the amount of MHV RNA were monitored at different time points (0, 24, and 48 h) post-treatment. RNA was extracted from all collected samples, and the levels of MHV and mouse glyceraldehyde-3-phosphate dehydrogenase (GAPDH) RNA were quantified by qPCR. Each RNA sample was analysed in triplicate, and the average copy number was calculated based on the mean Cq value from nine technical replicates ($n = 9$). Primers, probes, and the extended protocol are available in the Supplementary material (S2–3) and deposited at Zenodo [41].

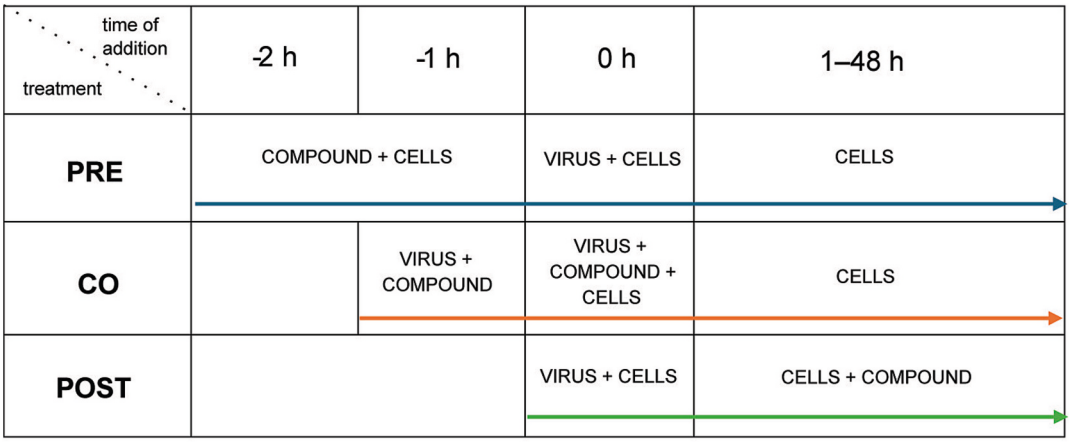

Fig. 3. Timeline of the Time-of-addition (ToA) assay. Pre-treatment (pre): cells were treated with the compound for 2 h prior to virus infection at 0 h, followed by infection for 1 h. Co-treatment (co): the compound and virus were co-incubated for 1 h before infecting the cells for 1 h. Post-treatment (post): cells were treated with the compound after virus infection for 1 h.

2.7. Light microscopy and transmission electron microscopy

The effects of MHV infection and LC treatment on L929 cells were observed using light microscopy and transmission electron microscopy. Four samples were prepared in parallel. The first sample (L929) served as the uninfected control and was cultured for 72 h. The second sample (L929 + MHV) was cultured under identical conditions for 24 h, then infected with MHV at an MOI of 0.001 for 1 h, followed by incubation for an additional 48 h. The third and fourth samples were treated with LC under post-treatment conditions: L929 + LC (LC-treated, uninfected cells) and L929 + MHV + LC (LC-treated cells infected with MHV at an MOI of 0.001 for 1 h). All samples were prepared in duplicate. At 48 h post-infection (hpi) cultures were harvested by scraping and immediately fixed in 3% glutaraldehyde in 0.1 M phosphate-buffered saline (PBS), post-fixed in 1% solution of osmium tetroxide for 1 h, followed by dehydration with ethanol and finally embedded in Agar 100 resin. Semithin and ultrathin sections were prepared with an Ultracut UC7 (Leica), using glass and diamond knives, respectively. Semithin sections were stained with toluidine blue and examined with a light microscope (Zeiss AxioSkop Opton) equipped with a digital camera (Leica DFC290HD; Leica Application Suite 4. 0. 0 Software). Ultrathin sections were stained with 1% (*w/v*) aqueous solution of uranyl acetate and lead citrate. The grids were then examined with a transmission electron microscope TALOS L120C (Thermo Scientific), operating at 100 kV and equipped with a Ceta 16 M camera.

2.8. Statistical analysis

The sigmoidal dose-response curve function (variable slope) was used to calculate the half-maximal effective concentration (EC_{50}) and cytotoxic concentration (CC_{50}). The ratio between CC_{50} and EC_{50} determines the selectivity index (SI). All data were plotted and analysed using GraphPad Prism software version 10.4.0 (USA). Results are presented as mean ± standard deviation. To calculate the statistical significance between control (infected samples, treated with 0.5% DMSO) and treatment (infected samples, treated with compounds) for qPCR results, a two-way analysis of variance (ANOVA) with Šidák's test, a multiple-comparison test, was conducted using GraphPad Prism software. Significance was reported for *p*-values < 0.05 (*), < 0.01 (**), < 0.001 (***) and ≤ 0.0001 (****). Additional information is available in the Supplementary material (S2).

3. Results

3.1. MD simulations and MM-PBSA analysis

The adamantane substructure query returned a focused set of FKKTLib entries containing the targeted scaffold. From these, we prioritised a lead candidate (LC) based on (i) unambiguous substructure match quality, (ii) availability of solid sample material for confirmation studies, and (iii) presence of coherent supporting annotations, yielding a well-characterised adamantane derivative as the most promising hit for subsequent evaluation.

LC, bound exclusively in the N-terminal vestibule (LC-N-Epro), was simulated in three independent 350 ns-long MD replicas. For rimantadine, the N-terminal vestibule complex (RMT-N-Epro) dissociated after ~140 ns and was therefore only simulated once, whereas the C-terminal vestibule complex (RMT-C-Epro) was simulated in three independent 200 ns-long replicas. The root mean square deviations (RMSD) calculated on the C-α atoms of Epro reached a stable state after ~75 ns (Fig. S1). In the case of RMT-N-Epro, the RMSD was already stable after 50 ns. The average plateau RMSD values ranged from 3.9 to 5.3 Å (Fig. S1), reflecting moderate structural flexibility characteristic of proteins with flexible loops and solvent-exposed regions. Importantly, this flexibility did not compromise channel integrity or ligand stability. Minor motions of the pentameric domains and ligand-induced conformational changes contributed to the overall RMSD, yet the protein's secondary-structure elements remained well conserved throughout the simulations. The radius of gyration was continuously stable over the simulated time, suggesting a stable assembly of the Epro ion channel (Fig. S2). The dissociation of RMT from the N-terminal is mainly attributed to shallow channel binding, weak hydrogen bonds, and limited van der Waals interactions with the amino acid residues. The channel is mainly a hydrophobic stretch, and only a few amino acid residues are responsible for the ligand-protein interactions (Fig. 4 and Table S2). In addition, the channel offers limited space, leading to steric conflicts between the residues and RMT within the N-terminal binding site. Therefore, the N-terminal vestibule was excluded from further analysis for RMT, and RMT was subsequently treated as a C-terminal binder only. The number of hydrogen bonds varied considerably for each candidate during the simulation (Fig. S3), indicating an overall higher number of hydrogen bonds for the lead candidate throughout the simulation. The highest populated clusters of the three replicas for LC

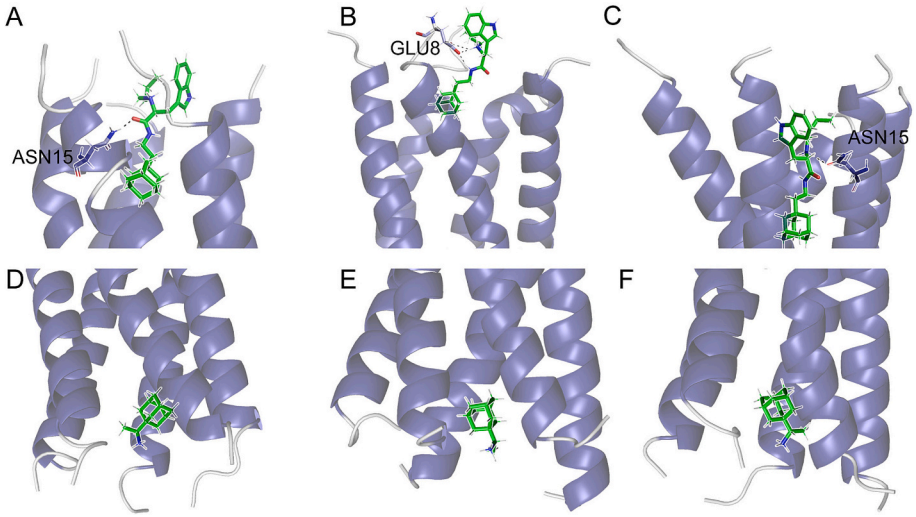

Fig. 4. Most representative clusters depicting hydrogen-bond interactions and binding poses of the final compound selection of LC-N-Epro (replicas 1–3 corresponding to **A**, **B**, and **C**) and RMT-C-Epro (replicas 1–3 corresponding to **D**, **E**, and **F**), respectively. Protein moieties are depicted in blue (α-helix) and white (disordered). The ligand is depicted in green. Nitrogen and oxygen atoms are depicted in blue and red, respectively. Hydrogen bonds are shown as dashed black lines. (For interpretation of the references to colour in this figure legend, the reader is referred to the web version of this article.)

Table 1
Total binding free energies, ΔG_{bind} and MD simulation durations.

MD run	ΔG_{bind} (kcal/mol)	Duration (ns)
LC N-terminal replica 1	−35 ± 4	350
LC N-terminal replica 2	−35 ± 7	350
LC N-terminal replica 3	−44 ± 4	350
RMT C-terminal replica 1	−22 ± 1	200
RMT C-terminal replica 2	−25 ± 2	200
RMT C-terminal replica 3	−21 ± 2	200

and RMT-C-Epro represent 91.8, 79.9, 75.7, 74.4, 84.3, and 94.0% of the equilibrated trajectory, respectively. Their protein-ligand interactions are described in the following text.

An MM-PBSA analysis was performed to rank the binding affinity of each ligand. The total binding free energies are listed in Table 1. LC consistently exhibits the strongest binding, followed by the RMT-C-Epro complexes. The ΔG_{bind} in the case of RMT was ~1.7-fold (C-terminal) lower than that of our lead candidate. At the amino acid residue level, GLU8 and THR11 were found to be major contributors to binding for LC (see Fig. S4 for the per-residue contributions), while the three runs showed differing extents of residue involvement.

Throughout two of the three simulations, LC displayed significant binding with one GLU8 side chain (Table S2); notably, this interaction was 6.7-fold and 2.2-fold stronger in the first run compared to the second and third runs, respectively. Furthermore, the third replica reports significant binding to two ASN15 residues and a LEU18 residue. Analysis of the highest populated clusters supports these findings (Fig. 4A–C) with the first and third replicas (rep-1 and rep-3) displaying a hydrogen bond between an ASN15 amine group and the carbonyl and secondary amine of LC's amide group, respectively, while the second replica (rep-2) displays a hydrogen bond between a GLU8 carboxy group and the amine of LC's amide group. Despite the microscopic differences between the three replicas, the MM-PBSA binding free energies for LC remain overall similar, indicating a small ensemble of distinct but comparably stable binding modes in which either C=O···H_2N@ASN15, NH···O=C@ASN15, or NH···O=C@GLU8 contacts serve as the primary anchor. Herein, the per-residue contributions for rep-1 and rep-3 point to a more mixed binding mode, with residues such as GLU8, THR9, THR11, and LEU18 contributing to binding. In contrast, rep-2 is strongly dominated by GLU8 (Fig. S4), whose persistent interaction across all runs further suggests a retainer-like role for GLU8 in suppressing axial drift and preventing dissociation from the N-terminal vestibule. We further note that in all replicas, LC's indole group and aliphatic chain face outwards from the channel, restricting hydrogen bonding to LC's amide and secondary amine. The adamantane moiety of LC penetrates deepest into the channel and exhibits a space-demanding and rigid geometry in which LC achieves an almost plug-like conformation in the channel. For RMT, no significant binding above 1.8 kcal/mol with any residue was observed at the C-terminal vestibule (Table S2). MM-PBSA analysis suggests relevant interactions with LEU28, ALA32, and THR35 residues. The structures of the highest populated clusters (Fig. 4D–F) do not show any hydrogen bonding for RMT at the C-terminal vestibule. Overall, RMT exhibits a space-demanding and rigid geometry, similarly to LC, effectively occupying space in the channel. In both cases, interactions appear to be dominated by their hydrophobic adamantane cores, with burial values indicating moderate channel penetration depths of (8 ± 2) Å and (6 ± 3) Å across runs for LC and RMT, respectively. While for RMT contacts *via* its amine group remain transient, LC seems to stabilise its binding *via* its amide group. In all simulations, the C-terminal ARG38 residues of the Epro homopentamer are consistently oriented towards the lipid–water interface and form salt bridges between their positively charged guanidinium groups and the negatively charged phosphate headgroups of

Table 2
Dose-response results of the tested compounds in L929 cells infected with MHV (MOI = 0.001). Mean of half-maximal effective (EC_{50}) and cytotoxic (CC_{50}) values with standard deviations (SD) are presented, calculated from three biological replicates ($N = 3$); the selectivity index (SI) was calculated as CC_{50}/EC_{50}. Cells were treated with the lead candidate (LC), 5-(*N*,*N*-hexamethylene)amiloride (HMA) or rimantadine (RMT) under post-treatment (post), co-treatment (co), and pre-treatment conditions.

COMPOUND (treatment)	CC_{50} (μM) (mean ± SD)	EC_{50} (μM) (mean ± SD)	SI
LC (post)	43 ± 1	12.7 ± 0.8	3.4
LC (co)		12 ± 1	3.6
LC (pre)		Not effective	/
HMA (post)	41 ± 2	7.6 ± 0.4	5.4
HMA (co)		14 ± 1	3.0
HMA (pre)		Not effective	/
RMT (post)	96 ± 5	26 ± 2	3.7
RMT (co)		Not effective	/
RMT (pre)		Not effective	/

the POPC bilayer. These interactions were persistent throughout the simulated timeframe and were observed in all monomers. Notably, in the C-terminal vestibule, the positively charged ligand RMT remained stably bound in close proximity to ARG38 throughout the simulations and did not dissociate from its binding site, despite the expected electrostatic repulsion between the positively charged groups.

3.2. Cytotoxicity and antiviral activity of the lead candidate against MHV

LC showed cytotoxic effects at concentrations above 30 μM, with a half-maximal cytotoxic concentration (CC_{50}) of 43 μM. The positive control HMA showed a comparable CC_{50} of 41 μM, while RMT was less cytotoxic, with a more than twofold higher CC_{50} of 96 μM (Table 2). Cytotoxic effects were evident at concentrations above 20 μM for HMA and 40 μM for RMT; however, the increase in cytotoxicity was more gradual for RMT compared to LC and HMA (Fig. 5A–F).

LC and the positive controls reduced MHV infectivity when added after infection of the cells with the virus (post-treatment) (Fig. 5A–C), with LC showing a half-maximal effective concentration (EC_{50}) of 12.7 μM and a selectivity index (SI) of 3.4. HMA and RMT showed EC_{50} values of 7.6 μM and 26 μM, resulting in SI values of 5.4 and 3.7, respectively (Table 2). When administered simultaneously with the virus (co-treatment), only LC and HMA showed antiviral activity (Fig. 5D–F). LC showed an EC_{50} of 12 μM and an SI of 3.6, which is very close to its efficacy under post-treatment conditions. HMA showed lower antiviral activity under co-treatment conditions (EC_{50} = 14 μM and SI of 3.0) and was about half as effective compared to post-treatment conditions. In contrast, RMT showed no activity at the concentrations tested under co-

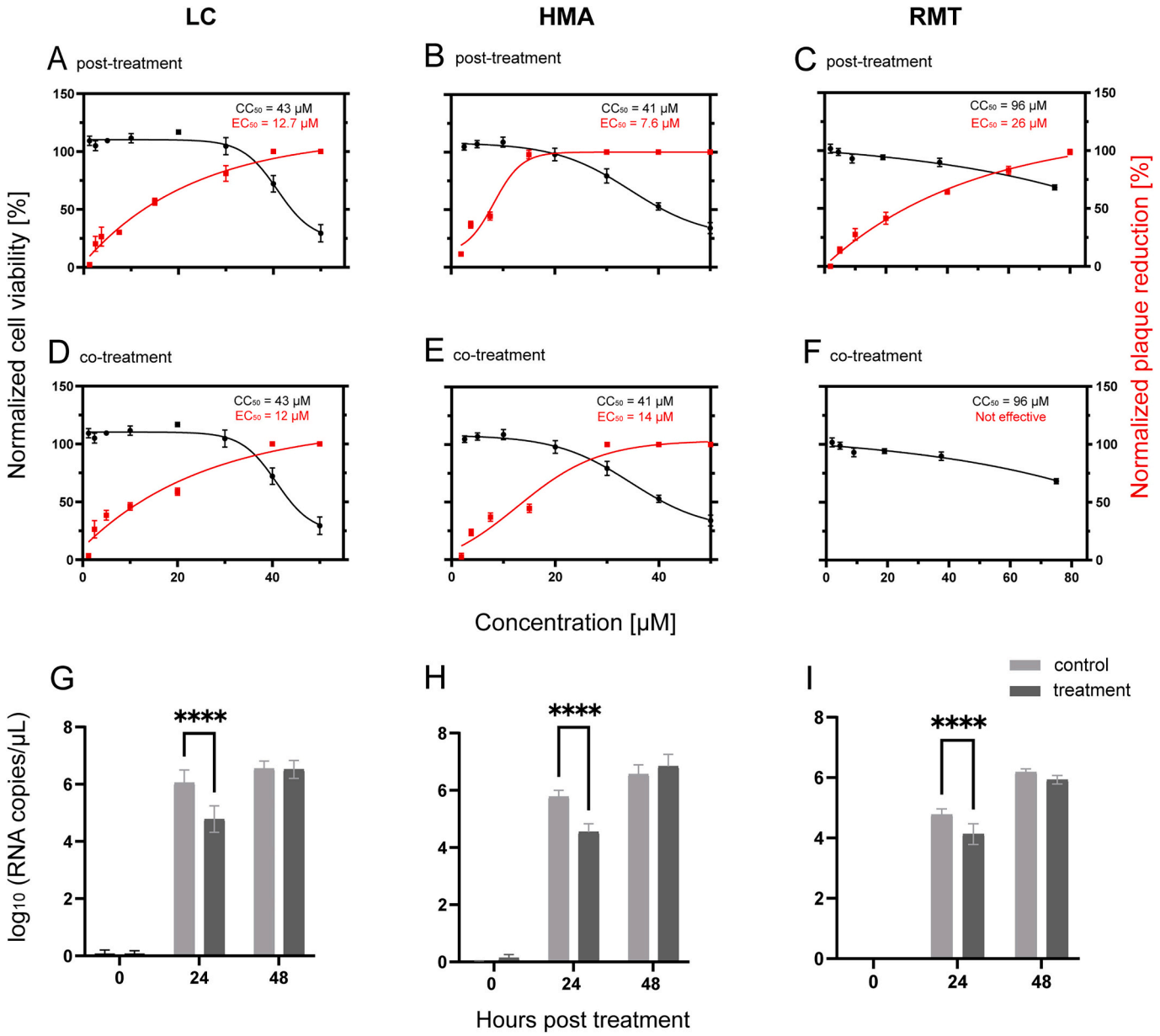

Fig. 5. Antiviral activity and effect on viral replication of LC, HMA, and RMT. **(A–F)** Results of plaque reduction assay and time-of-addition (ToA) assay for the lead candidate (LC; A, D) and the reference compounds 5-(*N*,*N*-hexamethylene)amiloride (HMA; B, E), and rimantadine (RMT; C, F), shown under post-treatment (upper panels) and co-treatment (lower panels) conditions. **(G–I)** Viral replication for the tested compounds (LC: G, HMA: H, RMT: I) at 0, 24, and 48 h post-treatment in log_{10}(RNA copies/μL). ****$P \leq 0.0001$ (two-way ANOVA, followed by Šidák's test). Detailed experimental conditions, normalization procedures, and statistical analyses are provided in the Supplementary material (S5).

treatment conditions. Importantly, none of the compounds reduced MHV infectivity when administered prior to virus infection under pre-treatment conditions. High repeatability (low variability) was observed in all three biological repetitions (Table 2).

3.3. The effect of the lead candidate on the viral replication of MHV

To follow viral replication, we performed quantitative PCR (qPCR) analysis following post-treatment with LC, HMA, and RMT. The RNA was extracted from combined cell lysates and supernatants collected at 0, 24, and 48 h post-treatment.

The absolute quantification of MHV RNA was enabled by a standard curve generated from a dilution series of a known viral RNA sample (6.5×10^5 copies/μL in the undiluted sample, corresponding to $10^{5.5}$ $TCID_{50}$/mL). The resulting standard curve showed a wide dynamic range over six orders of magnitude (slope = −3.35; intercept = 37.2; R^2 = 0.999), which enabled the accurate quantification of viral RNA in experimental samples.

As expected, the viral RNA levels in the infected cells increased over time. At 1 h post-infection (time point 0 h post-treatment), MHV RNA levels were close to the limit of detection (~1 copy/μL) for all treatments. By 24 h post-treatment, viral RNA levels increased by more than four orders of magnitude, reaching values of $5 \times 10^4 - 4 \times 10^6$ copies/μL in the positive controls (untreated infected samples). Importantly, treatment with LC resulted in a significant ~100-fold ($2 \log_{10}$) reduction in viral RNA compared to the positive control. A significant difference compared to the positive control was also observed for HMA and RMT. However, at 48 h post-treatment, RNA levels in the treated samples did not differ significantly from the positive control and peaked at 2×10^7 copies/μL (Fig. 5G–I). Additional information is available in the Supplementary material (S3–1).

3.4. Effects of the lead candidate on cell morphology and ultrastructure in MHV-infected cells

We analysed the effects of LC on MHV infectivity using light microscopy and transmission electron microscopy (TEM) 48 h post-infection (72 h after seeding), comparing four conditions: untreated cells (L929), infected cells (L929 + MHV), LC-treated uninfected cells (L929 + LC), and LC-treated infected cells (L929 + MHV + LC).

Light microscopy of semi-thin sections provided a general overview of the cell morphology (Fig. 6). Because the cells were harvested by scraping, the typical spindle-shaped morphology was lost; instead, cells appeared round to oval in all observed samples. In the L929 sample, the cell boundaries were clearly defined, and cell death was minimal (Fig. 6A). In contrast, in the L929 + MHV sample, most cells were dead, appearing as light-coloured patches, although the overall cell shape was largely preserved (Fig. 6B). Cell viability was markedly improved in

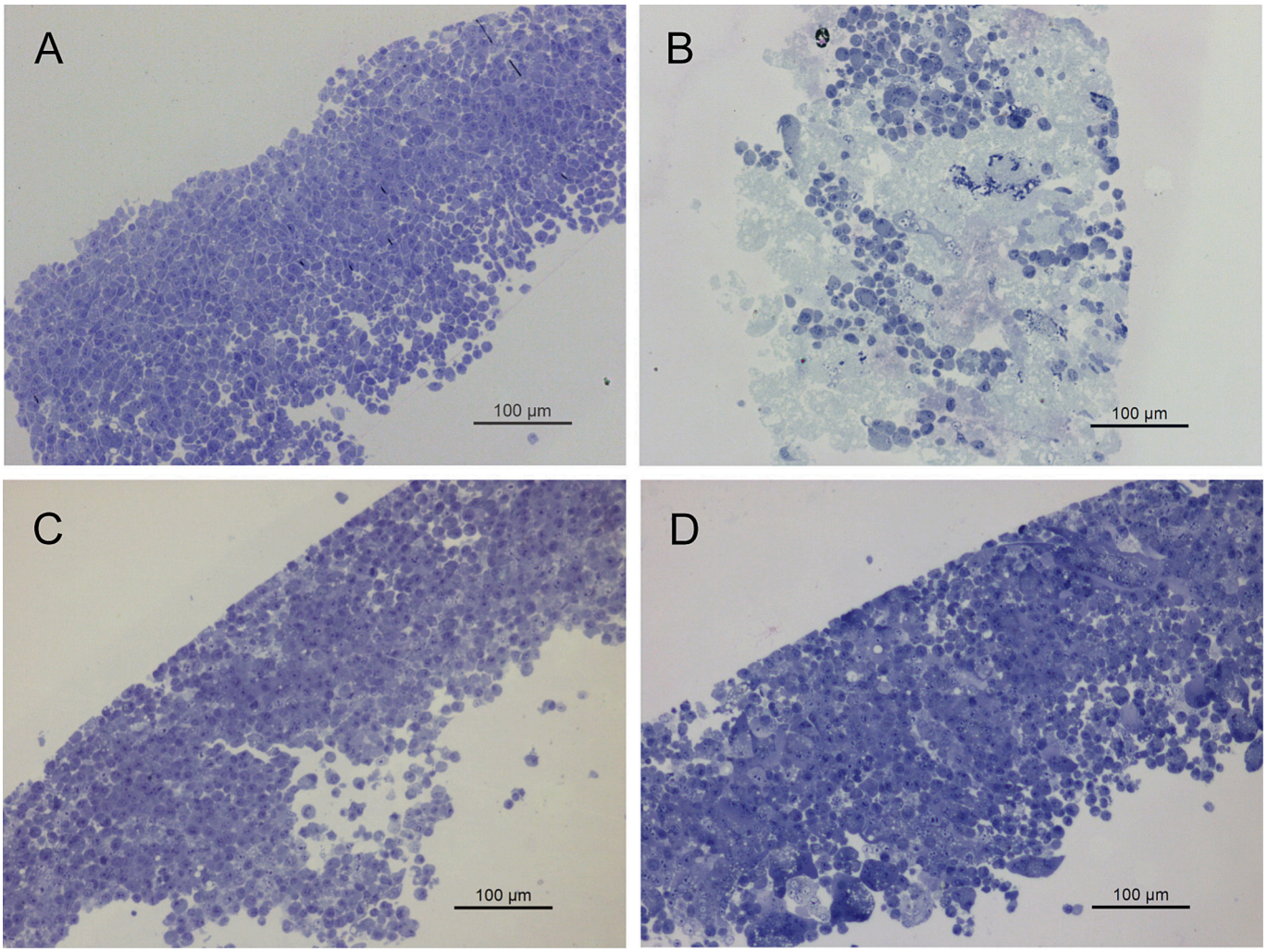

Fig. 6. Light microscopy of semi-thin sections. **(A)** Untreated cells (L929) with clearly defined cell boundaries and minimal cell death. **(B)** Infected cells (L929 + MHV) are dead (lighter and semi-transparent) with some viable cells (darker). **(C)** Uninfected cells treated with the LC (L929 + LC) and **(D)** infected cells treated with the LC (L929 + MHV + LC) both show minimal cell death and frequent cell-cell fusions with large multinucleated cells.

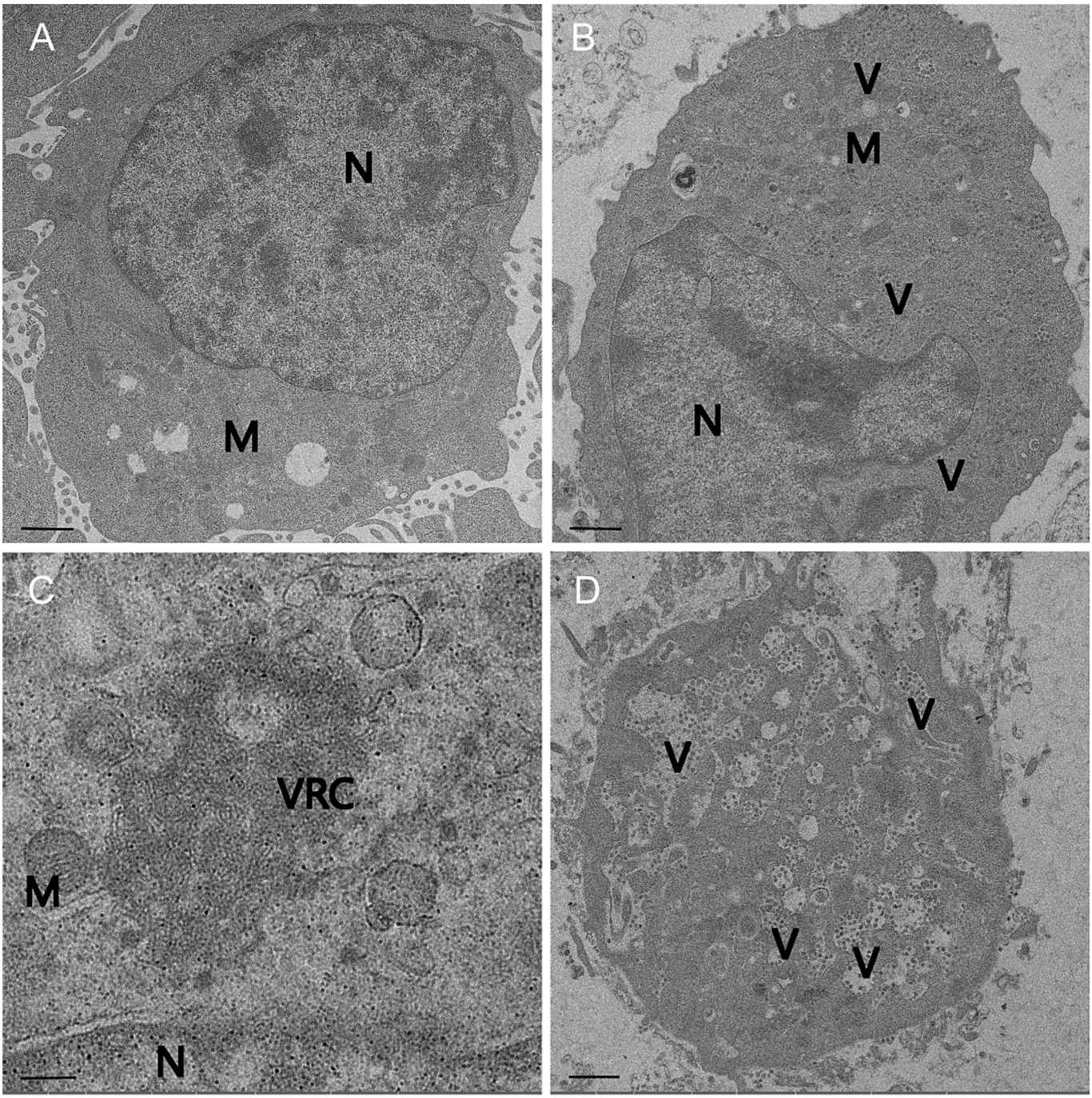

Fig. 7. Transmission electron microscopy (TEM). **(A)** Uninfected, untreated cells (L929), scale bar 1 μm. **(B)** Untreated infected cells (L929 + MHV), scale bar 1 μm. **(C)** Untreated infected cells (L929 + MHV), scale bar 200 nm. **(D)** Untreated infected cells (L929 + MHV), scale bar 1 μm. N: nucleus; V: viral particles; M: mitochondria; VRC: viral replication complex.

infected cells treated with LC (L929 + MHV + LC) (Fig. 6D). Treatment with LC, either alone or with infection, resulted in cell morphology largely similar to that of the uninfected control (L929). LC-treated samples frequently showed cell–cell fusions, producing large multinucleated cells, which may result from cytopathic effects at the concentration tested. Notably, this dose did not appear cytotoxic in the standard CCK-8 viability assay, which reflects cellular metabolic activity (Fig. 6C, D).

Ultrastructural analysis by TEM provided further insights into viral replication and cellular response. Untreated, uninfected cells (sample L929) had an electron-dense cytoplasm, numerous microvilli protruding from the entire surface, well-preserved mitochondria, endoplasmic reticulum (ER), and Golgi complexes, while membrane vesicles with myelin-like structures were observed only occasionally (Fig. 7A). Infected cells (sample L929 + MHV) showed extensive viral replication with widespread cytopathic effects. Numerous round to slightly oval virus particles with a diameter of about 65–80 nm were visible by TEM and were distributed both intracellularly and in the extracellular space (Fig. 7B–D). The spike proteins were not always clearly recognisable on the surface of the virions. Dead cells and cell debris, often interspersed with virus particles, predominated over viable cells. Despite the cytopathic damage, the cytoplasm of the infected cells remained electron-dense, with mitochondria preserved in large numbers. The cell nuclei were often more amoeboid in shape compared to those of uninfected

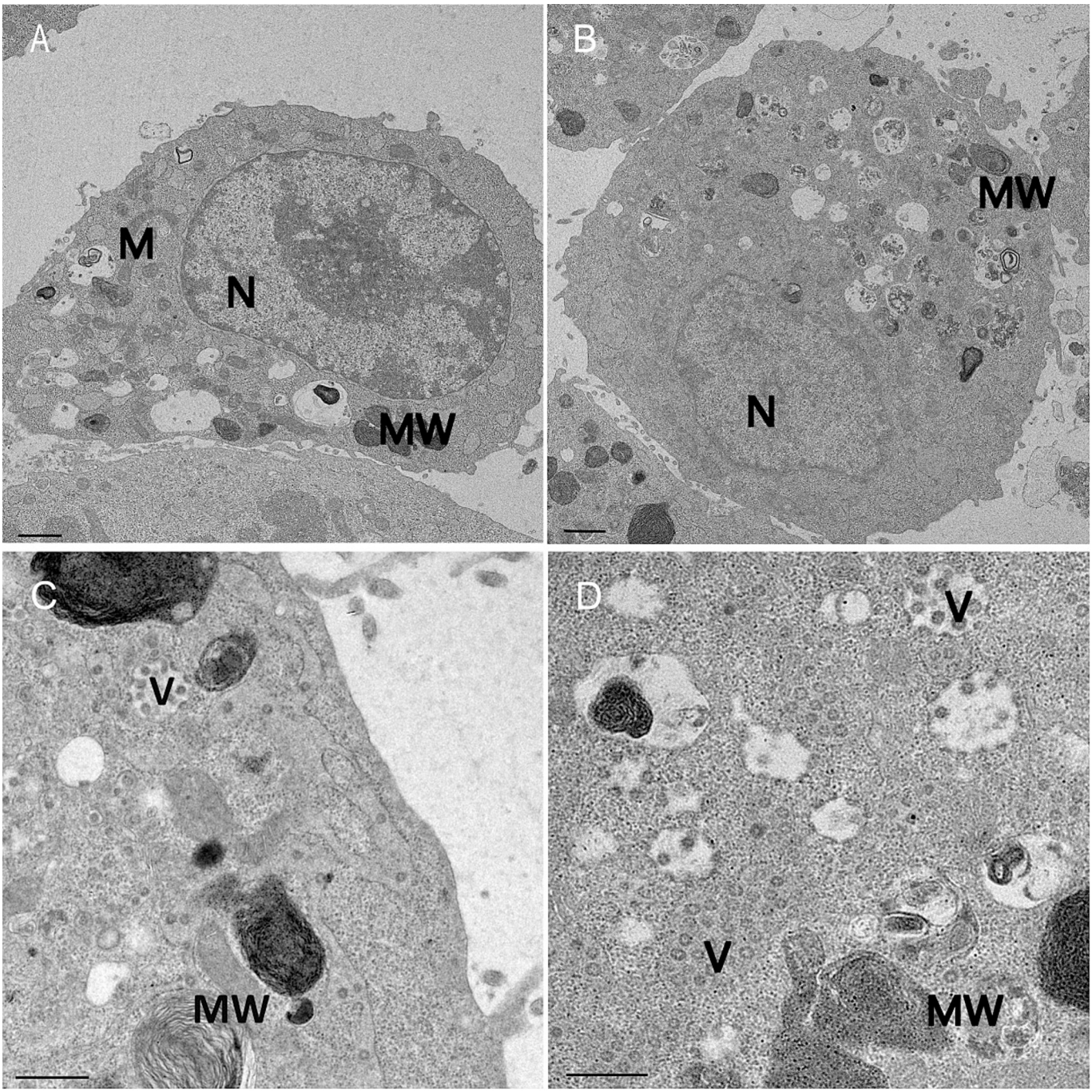

Fig. 8. Transmission electron microscopy (TEM). **(A)** Uninfected cells treated with the lead candidate (LC) (L929 + LC), scale bar 1 μm. **(B)** LC-treated infected cells (L929 + MHV + LC), scale bar 1 μm. **(C and D)** LC-treated infected cells (L929 + MHV + LC), scale bar 500 nm. N: nucleus; V: viral particles; M: mitochondria; MW: myelin-like whorls.

cells. Infected cells often contained abundant vesicles with viral particles, many of which appeared to originate from the ER. The size and morphology of these vesicles varied considerably in different sections, ranging from small, spherical structures to large, round or tubular compartments. In most of the cells, the ER appeared dilated. In addition, perinuclear regions resembling viral replication complexes or "viral factories" were frequently observed [42,43]. These structures, typically ~1 μm in diameter, had no bounding membrane and consisted of dense networks of short, disorganised tubes within a highly electron-dense matrix (Fig. 7C).

Treatment with LC (L929 + LC) led to the appearance of myelin-like membrane whorls within intracellular vesicles, which occurred more frequently than in untreated cells (sample L929) (Fig. 8A). Further information is available in the Supplementary material (S3–2). In LC-treated infected cells (L929 + MHV + LC), viral replication was still evident, as shown by the presence of replication complexes and vesicle-associated virus particles (Fig. 8B–D). The virus-induced changes in the cells were similar to those observed in untreated infected cells (L929 + MHV). In contrast to L929 + MHV, virus particles in LC-treated infected cells were mainly distributed intracellularly, while extracellular virions were rarely detected (Fig. 7D and Fig. 8B–C). Furthermore, virus particle semi-quantification was performed on multiple TEM sections, revealing a strong reduction in the number of extracellular particles in LC-treated samples compared to untreated infected cells (Table S3 and Fig. S6),

supporting the conclusion that LC restricts viral egress. We however, note that these values represent a semi-quantitative estimate rather than absolute virus particle numbers per cell.

4. Discussion

Despite advances in antiviral development, the rapid evolution of severe acute respiratory syndrome coronavirus 2 (SARS-CoV-2) continues to compromise drug efficacy [2,4,5,44], emphasising the need for therapeutics that are less susceptible to antiviral resistance. Among the structural proteins, SARS-CoV-2 envelope protein (Epro) has the lowest mutation frequency and the greatest resistance to mutagenic pressure [8–10,45]. Currently, the number of SARS-CoV-2 Epro inhibitors confirmed *in vitro* and *in vivo* is limited, and there are no approved COVID-19 drugs targeting this protein (Table S4) [46].

In this study, we identified a novel SARS-CoV-2 Epro inhibitor using an *in silico* approach and further characterised its antiviral activity against a model coronavirus (MHV) *in vitro*, showing EC_{50} values in the same general micromolar range as those of the known broad-spectrum coronavirus inhibitors 5-(*N*,*N*-hexamethylene)amiloride (HMA) and rimantadine (RMT).

HMA has been shown to be effective against several viroporin-forming viruses, including human immunodeficiency virus type 1 (HIV-1), influenza A virus (IAV), hepatitis C virus, and coronaviruses (CoVs) [25–28,47]. RMT, an aminoadamantane, is a well-characterised inhibitor of the matrix protein 2 (M2)of IAV. However, widespread resistance due to M2 mutations has led to being no longer used for the treatment of IAV [48]. Nevertheless, RMT retains its *in vitro* activity against both SARS-CoV-1 and SARS-CoV-2 by inhibiting Epro [7,31]. Despite this promising profile, no significant clinical benefit of RMT in patients with early-stage SARS-CoV-2 infection was observed in a large-scale observational study [49].

These findings point to the need for novel inhibitors with improved antiviral properties. As an initial step in this search, we performed *in silico* analyses to explore the potential of our lead candidate (LC), a functionalised adamantane linked to an indole group and an aliphatic chain *via* an amide linker.

4.1. Lead candidate forms stable complexes with the SARS-CoV-2 Epro N-terminal vestibule with high binding affinity

LC and RMT were subjected to classical MD simulations and MM-PBSA analysis. Clustering and MM-PBSA analysis of the SARS-CoV-2 Epro–ligand trajectories revealed relevant intermolecular interactions with the residues GLU8, THR9, THR11, ASN15, and LEU18 for LC, and with LEU28, ALA32, and THR35 for RMT. THR11 has been identified as a critical residue, engaging with experimentally confirmed inhibitors such as HMA and procyanidin [18,32]. Consistently, THR11ALA mutations of SARS-CoV-2 Epro result in a pronounced loss of ion channel currents and are associated with significantly reduced viral replication and virulence [20]. At the N-terminus, GLU8, an exposed residue, also interacts with procyanidin [32], and the flexible ring formed by its fivefold symmetry is thought to constitute an important regulatory component of the channel's cation selectivity filter [18]. In close proximity, THR9, a residue at the dynamic N-terminus, was found to strongly interact with HMA [18], supporting its importance as a residue for inhibitor binding. ASN15, the first pore-facing and channel-constricting residue at the N-terminus, has been reported to interact with several experimentally confirmed inhibitors, including HMA, AMT [18,31], and procyanidin [32]. Notably, ASN15ALA substitutions in SARS-CoV-1 Epro abolish ion conductance [18,50,51], underscoring its critical role in the channel's ion transport mechanism. LEU18, a hydrophobic residue, which forms a narrow stretch (pore radius of ~2 Å) of the channel along with LEU21, VAL25, and LEU28 [18], was found to interact strongly with other adamantanes such as adapalene and RLA-3107 as well as moderately with artefenomel [33]. Memantine and dopamantine (two adamantane derivatives) were found to interact with LEU28, ALA32, and THR35 residues, with both compounds binding at the C-terminal vestibule of the ion channel [33].

We further note that the persistent interactions of ARG38 with POPC headgroups suggest that the C-termini act as a membrane anchor that helps to stabilise the position and orientation of the Epro ion channel within the bilayer. By forming strong salt bridges with the lipid phosphate groups, ARG38 may effectively "lock" the C-terminal region at the membrane interface and pre-organise the C-terminal vestibule. Similarly, other viroporins are well known to anchor to the lipid bilayer by terminal positively charged residues such as lysine or arginine [52]. In this context, the stable binding of the positively charged RMT ligand in the immediate vicinity of ARG38, despite potential electrostatic repulsion, indicates that the overall local environment – comprising ARG38, nearby residues, and the lipid headgroups – creates a net stabilising interaction network. Thus, ARG38–lipid contacts may not only anchor the protein but also indirectly support the retention of positively charged ligands, such as RMT, at the C-terminal binding site. A mutational study by Steinmann et al. on the Hepatitis C virus p7 viroporin highlighted a similar role for conserved basic residues at the membrane interface, stabilising the proper orientation of the protein in the membrane *via* electrostatic interactions with the negatively charged phosphate groups of lipid headgroups. Upon replacement with neutral amino acids, production of infectious viral particles was dramatically suppressed, suggesting an important role for basic amino acid motifs positioned near the lipid headgroups at the membrane interface [53]. We note that the present simulations employ a simplified membrane model consisting of a homogeneous POPC bilayer. Real ERGIC/Golgi membranes are compositionally complex and may contain other components such as cholesterol and anionic lipids [54] that influence membrane properties and protein conformational equilibria. While such effects are not explicitly captured here, the chosen model allows for controlled and reproducible comparison of ligand binding within a consistent environment. The incorporation of lipid heterogeneity thus represents an important direction for future studies. The MD simulations performed indicate that LC and RMT block the SARS-CoV-2 Epro ion channel over an extended period of time by forming stable complexes at the N-terminal and C-terminal vestibules, respectively. Binding affinities were calculated for these candidates, with LC outperforming the positive control compound RMT by a factor of 1.7. We note that the C- and N-terminal vestibules face the cytoplasm and ERGIC lumen, respectively; thus, binding-site preference could modulate both blockade efficacy and compartmental access. However, a detailed elucidation of its pharmacodynamic implications is outside the scope of this study.

4.2. The lead candidate inhibits MHV infectivity

MHV is used as a surrogate because it is a close phylogenetic relative of SARS-CoV-2; both viruses share similar structural features, exhibit comparable infection-related pathogenic processes, and can cause similar severe pathological outcomes [36,55,56]. LC reduced MHV infectivity *in vitro* in a dose-dependent manner and showed strong antiviral activity with an EC_{50} of 12 μM, as confirmed by plaque reduction assay experiments. LC exhibited selectivity indexes of a similar order to those of RMT and HMA in this assay system, highlighting its efficacy as a competitive antiviral candidate. Time-of-addition (ToA) experiments indicated that all three compounds act in the late stages of the MHV life cycle, which is consistent with previous findings and the known role of Epro [57,58]. In addition, the potent activities of LC and HMA at co-treatment suggest that they either interfere with the early stages of viral entry or interact with virus particles in a virucidal manner, possibly inactivating the virus before cellular infection [59].

Regarding the antiviral efficacy of HMA and RMT, our results are consistent with previous reports describing similar efficacy values [27,60]. Breitinger et al. [7,31] also showed that HMA, RMT, and AMT

inhibit both SARS-CoV-1 and SARS-CoV-2 Epro *in vitro*, with HMA being the most potent – a trend reflected in our results. The ratio of RMT's and HMA's EC_{50} values in our study (3.4) is comparable to previously reported ratios for SARS-CoV-2 Epro (6) and SARS-CoV-1 Epro (4) and underscores consistency across CoVsand experimental systems, despite methodological differences [7,31]. Further, RMT was found to be less cytotoxic than HMA, consistent with previous studies showing that adamantanes such as RMT and AMT generally have lower cytotoxicity [7,61,62].

4.3. The lead candidate transiently delays viral RNA replication

We observed that viral RNA replication was delayed in infected cells treated with LC. Significantly lower RNA levels were detected after 24 h compared to untreated infected controls. Similar results were observed for HMA and RMT, indicating that Epro plays a role in viral replication, although the tested inhibitors did not completely block viral replication. Kuo et al. [11] and DeDiego et al. [63] reported that MHV and SARS-CoV-1 *E*-gene deletion mutants had infectious titres three orders of magnitude lower, as demonstrated *in vitro* and *in vivo*, concluding that Epro is critical but not essential for viral replication [11,63]. Previous studies show that SARS-CoV-1 Epro contributes to virulence, particularly through the PDZ-binding motif (PBM), a C-terminal domain involved in protein–protein interactions and modulation of signalling pathways involved in pathogenesis [64]. Alvarez et al. [65] reported that SARS-CoV-2 PBM mutants exhibit delayed replication (at 24 and 32 h post-infection) *in vitro* and cause less weight loss, lower viral load, significantly attenuated inflammatory responses, and milder respiratory damage *in vivo* [65]. Similarly, reduced lung inflammation was reported for SARS-CoV-1 Epro mutants *in vivo* [63]. Taken together, these results suggest that Epro's contribution to virulence cannot be explained by replication efficiency alone but is closely linked to inflammation.

4.4. The lead candidate prevents cell lysis by attenuating virus release

Light microscopy and TEM analysis showed that LC strongly reduces virion release and consequently prevents cell lysis. Consistent with our qPCR results, LC did not affect viral genome replication at 48 hpi, as we observed virus-induced changes comparable to the positive control. Similarly, Ortega et al. [66] reported that despite successful viral genome replication, deletion of Epro in transmissible gastroenteritis coronavirus led to two distinct effects: blockade of virus transport in the membranes of the secretory pathway and impaired virion maturation. As in our study, an accumulation of virions in intracellular compartments was observed, supporting a role of Epro in virus post-replication phases. Recent work also shows that β-CoVs use lysosomes for egress, with Epro migrating from the Golgi to the lysosomes, where its viroporin activity inhibits acidification and promotes efficient virus release [67–70]. According to Pearson et al. [68], mutations in the C-terminal region of SARS-CoV-2 Epro cause it to remain in the endoplasmic reticulum, thereby hindering its transport to the lysosomes. The conserved hydrophobic residues in the C-terminal region suggest that ER export is a universal CoV mechanism that enables viral assembly [68]. Despite evidence that Epro cooperates with M protein to ensure efficient assembly [71], studies have shown that expression of Epro alone can drive vesicle formation and induce membranous structures resembling those in infected cells, suggesting that it can act independently of other viral components [13,72,73], emphasising the essential role of Epro in morphogenesis, maturation, assembly, and release of virions.

The observed consensus between *in silico* and *in vitro* results suggests that LC is a potent candidate for inhibiting the SARS-CoV-2 Epro ion channel. Herein, our study builds directly on our previous *in silico* work on the SARS-CoV-2 Epro ion channel, applying the same MD and MM-PBSA protocol to enable a like-for-like comparison. Our current lead candidate shows the highest calculated binding affinity among all prior hits, surpassing our previously identified lead compounds (L2 and L3) and rimantadine [34]. Specifically, LC forms stable protein–drug complexes at the N-terminal vestibule of the SARS-CoV-2 Epro ion channel, interacting with the key residues GLU8, THR9, THR11, ASN15, and LEU18 and showing a more favourable calculated binding affinity than rimantadine under the present simulation conditions. Our findings suggest that inhibition of Epro channel function impairs viral egress and the subsequent spread of infectious virus particles, resulting in delayed RNA replication and reduced overall infectivity. Consistent with this mechanism, LC not only protects infected cells from virus-induced death but also limits transmission to surrounding uninfected cells. This combined effect – preserving cell integrity while restricting viral spread – strongly supports the potential of LC as a promising lead compound for the development of new coronavirus therapeutics.

Current antiviral strategies, shaped by previous outbreaks of SARS-CoV and Middle East respiratory syndrome coronavirus, essentially follow two complementary approaches: direct inhibition of the viral life cycle and modulation of the host's inflammatory response, which plays a crucial role in disease severity [74,75]. Epro inhibitors represent a distinct therapeutic class that acts *via* both mechanisms – interfering with the viral assembly and release while modulating host cell processes. This dual mode of action emphasises their potential as promising candidates for the development of next-generation antiviral agents against SARS-CoV-2 and other β-CoVs, as these viruses share similar structural features and exhibit high sequence homology across multiple conserved domains [35,36,76].

5. Conclusions

In this study, we identified and characterised a novel potential inhibitor of the SARS-CoV-2 Epro ion channel, a highly conserved viroporin crucial for viral assembly, release, and pathogenesis. We demonstrated the antiviral activity of our lead candidate against MHV, a surrogate virus for SARS-CoV-2 and other β-CoVs. By integrating three complementary *in vitro* approaches, we gained deeper insight into the mechanism of action and virus–cell interaction. Furthermore, *in silico* analyses using molecular dynamics simulations and MM-PBSA calculations identified our compound as a promising inhibitor of SARS-CoV-2 Epro, emphasising its potential for further preclinical development.

Although MHV is a useful surrogate betacoronavirus model, differences in envelope protein structure and viral dynamics across CoVs may limit direct extrapolation to SARS-CoV-2. Accordingly, complementary studies – including live-cell imaging, electrophysiology, *in vitro* validation in authentic SARS-CoV-2 and/or other relevant human coronavirus systems, and *in vivo* evaluation – will be important next steps to further assess the efficacy, pharmacokinetics, and safety profile of LC. In parallel, structural optimisation of LC, to improve its safety profile and enhance antiviral activity, will be a key focus of future development. These studies will provide crucial insights into its therapeutic potential and tolerability in a physiological context. The approach employed and the findings presented in this study could be a valuable addition to the currently limited repertoire of antiviral drugs available for the treatment of COVID-19 and other emerging coronavirus-related diseases.

CRediT authorship contribution statement

Nina Kobe: Writing – review & editing, Writing – original draft, Visualization, Validation, Software, Methodology, Investigation, Formal analysis, Data curation, Conceptualization. **Lennart Dreisewerd:** Writing – review & editing, Visualization, Validation, Software, Methodology, Investigation, Formal analysis, Data curation. **Miha Lukšič:** Writing – review & editing, Visualization, Validation, Software, Resources, Methodology, Investigation, Formal analysis, Data curation. **Matic Pavlin:** Writing – review & editing, Visualization, Validation, Software, Methodology, Investigation, Formal analysis. **Uroš Grošelj:** Writing – review & editing, Visualization, Validation, Resources. **Črtomir Podlipnik:** Writing – review & editing, Validation,

Methodology. **Mojca Janc:** Writing – review & editing, Visualization, Software, Methodology. **Živa Lengar:** Writing – review & editing, Validation, Software, Methodology. **Polona Mrak:** Writing – review & editing, Validation, Software, Methodology. **Magda Tušek Žnidarič:** Writing – review & editing, Visualization, Validation, Methodology, Investigation, Formal analysis. **Maruša Pompe Novak:** Writing – review & editing, Funding acquisition. **Urška Kuhar:** Writing – review & editing. **Peter Hostnik:** Writing – review & editing. **Federica Dattola:** Writing – review & editing. **Tea Carletti:** Writing – review & editing. **Alessandro Marcello:** Writing – review & editing. **Polona Kogovšek:** Writing – review & editing, Supervision, Funding acquisition, Conceptualization.

Declaration of competing interest

The authors declare that they have no known competing financial interests or personal relationships that could have appeared to influence the work reported in this paper.

Acknowledgments

The authors acknowledge the financial support from The Slovenian Research and Innovation Agency (research core funding Nos. P4-0463 (N.K., P.K., Ž.L., M.J., M.T.Ž.), P4-0165 (M.P.N.), P2-0152 (L.D.), P2-0421 (M.P.), P1-0179 (U.G.), P1-0201 (M.L., Č.P.) and P4-0092 (U.K., P. H.)), the Erasmus+ Programme of the European Union (2023-1-SI01-KA131-HED-000122972), intramural funding scheme of the ICGEB, the Italian National Institute of Health (ISS) grant RIPREI2023 and the Geissblatt Stiftung (Lichtenstein). The authors acknowledge the support of the Centre for Research Infrastructure at the UL FKKT, which is part of the Network of Research and Infrastructural Centres UL (MRIC UL) and is financially supported by the ARIS (Infrastructure programme No. I0-0022). The authors also acknowledge the Ažman high-performance computing (HPC) centre at the National Institute of Chemistry and HPC RIVR consortium (HPC Vega) for computing resources. Figure 1 and the graphical abstract have been created with BioRender.com. We thank Luka Ciber, Maja Ferle, and Ema Mrhar for laboratory assistance.

Appendix A. Supplementary data

Supplementary data to this article can be found online at https://doi.org/10.1016/j.bioorg.2026.109949.

Data availability

I have chared the link to all the data.

References

[1] Y. Mahmoud, A. Hathout, R.A. Amen, S. Desouky, R.M. Shady, H.M. Fahmy, COVID-19 Omicron variant: variation from other variants, immune response, and vaccination against this rapidly spreading pandemic, Rev. Res. Med. Microbiol. 36 (2025) 38–47, https://doi.org/10.1097/MRM.0000000000000386.

[2] S. Gandhi, J. Klein, A.J. Robertson, M.A. Peña-Hernández, M.J. Lin, P. Roychoudhury, P. Lu, J. Fournier, D. Ferguson, S.A.K. Mohamed Bakhash, M. Catherine Muenker, A. Srivathsan, E.A. Wunder, N. Kerantzas, W. Wang, B. Lindenbach, A. Pyle, C.B. Wilen, O. Ogbuagu, A.L. Greninger, A. Iwasaki, W. L. Schulz, A.I. Ko, De novo emergence of a remdesivir resistance mutation during treatment of persistent SARS-CoV-2 infection in an immunocompromised patient: a case report, Nat. Commun. 13 (2022) 1547, https://doi.org/10.1038/s41467-022-29104-y.

[3] T. Sanderson, R. Hisner, I. Donovan-Banfield, H. Hartman, A. Løchen, T.P. Peacock, C. Ruis, A molnupiravir-associated mutational signature in global SARS-CoV-2 genomes, Nature 623 (2023) 594–600, https://doi.org/10.1038/s41586-023-06649-6.

[4] Y. Duan, H. Zhou, X. Liu, S. Iketani, M. Lin, X. Zhang, Q. Bian, H. Wang, H. Sun, S. J. Hong, B. Culbertson, H. Mohri, M.I. Luck, Y. Zhu, X. Liu, Y. Lu, X. Yang, K. Yang, Y. Sabo, A. Chavez, S.P. Goff, Z. Rao, D.D. Ho, H. Yang, Molecular mechanisms of SARS-CoV-2 resistance to nirmatrelvir, Nature 622 (2023) 376–382, https://doi.org/10.1038/s41586-023-06609-0.

[5] N.R. Aggarwal, K.C. Molina, L.E. Beaty, T.D. Bennett, N.E. Carlson, D.A. Mayer, J. L. Peers, S. Russell, M.K. Wynia, A.A. Ginde, Real-world use of nirmatrelvir–ritonavir in outpatients with COVID-19 during the era of omicron variants including BA.4 and BA.5 in Colorado, USA: a retrospective cohort study, Lancet Infect. Dis. 23 (2023) 696–705, https://doi.org/10.1016/S1473-3099(23)00011-7.

[6] S. Zhou, P. Lv, M. Li, Z. Chen, H. Xin, S. Reilly, X. Zhang, SARS-CoV-2 E protein: pathogenesis and potential therapeutic development, Biomed. Pharmacother. 159 (2023) 114242, https://doi.org/10.1016/j.biopha.2023.114242.

[7] U. Breitinger, C.A. Sedky, H. Sticht, H.-G. Breitinger, Patch-clamp studies and cell viability assays suggest a distinct site for viroporin inhibitors on the E protein of SARS-CoV-2, Virol. J. 20 (2023) 142, https://doi.org/10.1186/s12985-023-02095-y.

[8] S. Laha, J. Chakraborty, S. Das, S.K. Manna, S. Biswas, R. Chatterjee, Characterizations of SARS-CoV-2 mutational profile, spike protein stability and viral transmission, Infect. Genet. Evol. 85 (2020) 104445, https://doi.org/10.1016/j.meegid.2020.104445.

[9] D. Chaudhuri, S. Majumder, J. Datta, K. Giri, In silico study of mutational stability of SARS-CoV-2 proteins, Protein J. 40 (2021) 328–340, https://doi.org/10.1007/s10930-021-09988-3.

[10] O.E. Omotoso, J.O. Olugbami, M.A. Gbadegesin, Assessment of intercontinents mutation hotspots and conserved domains within SARS-CoV-2 genome, Infect. Genet. Evol. 96 (2021) 105097, https://doi.org/10.1016/j.meegid.2021.105097.

[11] L. Kuo, P.S. Masters, The small envelope protein E is not essential for murine coronavirus replication, J. Virol. 77 (2003) 4597–4608, https://doi.org/10.1128/JVI.77.8.4597-4608.2003.

[12] J.L. Nieto-Torres, M.L. DeDiego, E. Álvarez, J.M. Jiménez-Guardeño, J.A. Regla-Nava, M. Llorente, L. Kremer, S. Shuo, L. Enjuanes, Subcellular location and topology of severe acute respiratory syndrome coronavirus envelope protein, Virology 415 (2011) 69–82, https://doi.org/10.1016/j.virol.2011.03.029.

[13] M.J.B. Raamsman, J.K. Locker, A. De Hooge, A.A.F. De Vries, G. Griffiths, H. Vennema, P.J.M. Rottier, Characterization of the coronavirus mouse hepatitis virus strain A59 small membrane protein E, J. Virol. 74 (2000) 2333–2342, https://doi.org/10.1128/JVI.74.5.2333-2342.2000.

[14] F. Fischer, C.F. Stegen, P.S. Masters, W.A. Samsonoff, Analysis of constructed E gene mutants of mouse hepatitis virus confirms a pivotal role for E protein in coronavirus assembly, J. Virol. 72 (1998) 7885–7894, https://doi.org/10.1128/JVI.72.10.7885-7894.1998.

[15] K.M. Curtis, B. Yount, R.S. Baric, Heterologous gene expression from transmissible gastroenteritis virus replicon particles, J. Virol. 76 (2002) 1422–1434, https://doi.org/10.1128/JVI.76.3.1422-1434.2002.

[16] C. Castaño-Rodriguez, J.M. Honrubia, J. Gutiérrez-Álvarez, M.L. DeDiego, J. L. Nieto-Torres, J.M. Jimenez-Guardeño, J.A. Regla-Nava, R. Fernandez-Delgado, C. Verdia-Báguena, M. Queralt-Martín, G. Kochan, S. Perlman, V.M. Aguilella, I. Sola, L. Enjuanes, Role of severe acute respiratory syndrome coronavirus viroporins E, 3a, and 8a in replication and pathogenesis, mBio 9 (2018) e02325-17, https://doi.org/10.1128/mBio.02325-17.

[17] P. Venkatagopalan, S.M. Daskalova, L.A. Lopez, K.A. Dolezal, B.G. Hogue, Coronavirus envelope (E) protein remains at the site of assembly, Virology 478 (2015) 75–85, https://doi.org/10.1016/j.virol.2015.02.005.

[18] V.S. Mandala, M.J. McKay, A.A. Shcherbakov, A.J. Dregni, A. Kolocouris, M. Hong, Structure and drug binding of the SARS-CoV-2 envelope protein transmembrane domain in lipid bilayers, Nat. Struct. Mol. Biol. 27 (2020) 1202–1208, https://doi.org/10.1038/s41594-020-00536-8.

[19] D. Cabrera-Garcia, R. Bekdash, G.W. Abbott, M. Yazawa, N.L. Harrison, The envelope protein of SARS-CoV-2 increases intra-Golgi pH and forms a cation channel that is regulated by pH, J. Physiol. 599 (2021) 2851–2868, https://doi.org/10.1113/JP281037.

[20] B. Xia, X. Shen, Y. He, X. Pan, F.-L. Liu, Y. Wang, F. Yang, S. Fang, Y. Wu, Z. Duan, X. Zuo, Z. Xie, X. Jiang, L. Xu, H. Chi, S. Li, Q. Meng, H. Zhou, Y. Zhou, X. Cheng, X. Xin, L. Jin, H.-L. Zhang, D.-D. Yu, M.-H. Li, X.-L. Feng, J. Chen, H. Jiang, G. Xiao, Y.-T. Zheng, L.-K. Zhang, J. Shen, J. Li, Z. Gao, SARS-CoV-2 envelope protein causes acute respiratory distress syndrome (ARDS)-like pathological damages and constitutes an antiviral target, Cell Res. 31 (2021) 847–860, https://doi.org/10.1038/s41422-021-00519-4.

[21] D.R. Hout, M.L. Gomez, E. Pacyniak, L.M. Gomez, B. Fegley, E.R. Mulcahy, M. S. Hill, N. Culley, D.M. Pinson, W. Nothnick, M.F. Powers, S.W. Wong, E. B. Stephens, Substitution of the transmembrane domain of Vpu in simian–human immunodeficiency virus (SHIVKU1bMC33) with that of M2 of influenza a results in a virus that is sensitive to inhibitors of the M2 ion channel and is pathogenic for pig-tailed macaques, Virology 344 (2006) 541–559, https://doi.org/10.1016/j.virol.2005.08.022.

[22] D.R. Hout, M.L. Gomez, E. Pacyniak, L.M. Gomez, S.H. Inbody, E.R. Mulcahy, N. Culley, D.M. Pinson, M.F. Powers, S.W. Wong, E.B. Stephens, Scrambling of the amino acids within the transmembrane domain of Vpu results in a simian-human immunodeficiency virus (SHIVTM) that is less pathogenic for pig-tailed macaques, Virology 339 (2005) 56–69, https://doi.org/10.1016/j.virol.2005.04.038.

[23] M. Takeda, A. Pekosz, K. Shuck, L.H. Pinto, R.A. Lamb, Influenza a virus M_2 ion channel activity is essential for efficient replication in tissue culture, J. Virol. 76 (2002) 1391–1399, https://doi.org/10.1128/JVI.76.3.1391-1399.2002.

[24] T. Sakaguchi, G.P. Leser, R.A. Lamb, The ion channel activity of the influenza virus M2 protein affects transport through the Golgi apparatus, J. Cell Biol. 133 (1996) 733–747, https://doi.org/10.1083/jcb.133.4.733.

[25] G.D. Ewart, K. Mills, G.B. Cox, P.W. Gage, Amiloride derivatives block ion channel activity and enhancement of virus-like particle budding caused by HIV-1 protein Vpu, Eur. Biophys. J. 31 (2002) 26–35, https://doi.org/10.1007/s002490100177.

[26] P.H. Jalily, J. Eldstrom, S.C. Miller, D.C. Kwan, S.S.-H. Tai, D. Chou, M. Niikura, I. Tietjen, D. Fedida, Mechanisms of action of novel influenza a/M2 viroporin inhibitors derived from hexamethylene amiloride, Mol. Pharmacol. 90 (2016) 80–95, https://doi.org/10.1124/mol.115.102731.
[27] L. Wilson, P. Gage, G. Ewart, Hexamethylene amiloride blocks E protein ion channels and inhibits coronavirus replication, Virology 353 (2006) 294–306, https://doi.org/10.1016/j.virol.2006.05.028.
[28] A. Premkumar, L. Wilson, G.D. Ewart, P.W. Gage, Cation-selective ion channels formed by p7 of hepatitis C virus are blocked by hexamethylene amiloride, FEBS Lett. 557 (2004) 99–103, https://doi.org/10.1016/S0014-5793(03)01453-4.
[29] V.M. Deyde, X. Xu, R.A. Bright, M. Shaw, C.B. Smith, Y. Zhang, Y. Shu, L. V. Gubareva, N.J. Cox, A.I. Klimov, Surveillance of resistance to adamantanes among influenza a(H3N2) and a(H1N1) viruses isolated worldwide, J. Infect. Dis. 196 (2007) 249–257, https://doi.org/10.1086/518936.
[30] P. Intharathep, C. Laohpongspaisan, T. Rungrotmongkol, A. Loisruangsin, M. Malaisree, P. Decha, O. Aruksakunwong, K. Chuenpennit, N. Kaiyawet, P. Sompornpisut, S. Pianwanit, S. Hannongbua, How amantadine and rimantadine inhibit proton transport in the M2 protein channel, J. Mol. Graph. Model. 27 (2008) 342–348, https://doi.org/10.1016/j.jmgm.2008.06.002.
[31] U. Breitinger, N.K.M. Ali, H. Sticht, H.-G. Breitinger, Inhibition of SARS CoV envelope protein by flavonoids and classical viroporin inhibitors, Front. Microbiol. 12 (2021) 692423, https://doi.org/10.3389/fmicb.2021.692423.
[32] Y. Wang, S. Fang, Y. Wu, X. Cheng, L. Zhang, X. Shen, S. Li, J. Xu, W. Shang, Z. Gao, B. Xia, Discovery of SARS-CoV-2-E channel inhibitors as antiviral candidates, Acta Pharmacol. Sin. 43 (2022) 781–787, https://doi.org/10.1038/s41401-021-00732-2.
[33] S. Yousefbeigi, F. Marsusi, Advanced computational approaches to evaluate the potential of new-generation adamantane-based drugs as Viroporin inhibitors: a case study on SARS-CoV-2, J. Phys. Chem. B 129 (2025) 8127–8143, https://doi.org/10.1021/acs.jpcb.5c02898.
[34] N. Kobe, L. Dreisewerd, M. Pavlin, P. Kogovšek, Č. Podlipnik, U. Grošelj, M. Lukšič, In silico determination of novel SARS-CoV-2 envelope protein ion channel inhibitors, Comput. Struct. Biotechnol. J. (2025), https://doi.org/10.1016/j.csbj.2025.06.036. S2001037025002557.
[35] W. Cui, S. Cui, C. Chen, X. Chen, Z. Wang, H. Yang, L. Zhang, The crystal structure of main protease from mouse hepatitis virus A59 in complex with an inhibitor, Biochem. Biophys. Res. Commun. 511 (2019) 794–799, https://doi.org/10.1016/j.bbrc.2019.02.105.
[36] F.-Y. Nan, C.-J. Wu, J.-H. Su, L.-Q. Ma, Potential mouse models of coronavirus-related immune injury, Front. Immunol. 13 (2022) 943783, https://doi.org/10.3389/fimmu.2022.943783.
[37] T. Shuipys, N. Montazeri, Optimized protocols for the propagation and quantification of infectious murine hepatitis virus (MHV-A59) using NCTC clone 1469 and 929 cells, Methods Protoc. 5 (2022), https://doi.org/10.3390/mps5010005.
[38] B. Yount, M.R. Denison, S.R. Weiss, R.S. Baric, Systematic assembly of a full-length infectious cDNA of mouse hepatitis virus strain A59, J. Virol. 76 (2002) 11065–11078, https://doi.org/10.1128/JVI.76.21.11065-11078.2002.
[39] L.J. Reed, H. Muench, A simple method of estimating fifty per cent endpoints12, Am. J. Epidemiol. 27 (1938) 493–497, https://doi.org/10.1093/oxfordjournals.aje.a118408.
[40] A. Meden, D. Knez, M. Jukič, X. Brazzolotto, M. Gršič, A. Pišlar, A. Zahirović, J. Kos, F. Nachon, J. Svete, S. Gobec, U. Grošelj, Tryptophan-derived butyrylcholinesterase inhibitors as promising leads against Alzheimer's disease, Chem. Commun. 55 (2019) 3765–3768, https://doi.org/10.1039/C9CC01330J.
[41] N. Kobe, L. Dreisewerd, M. Lukšič, M. Pavlin, Č. Podlipnik, Grošelj, Uroš, M. Janc, Ž. Lengar, P. Mrak, M. Tušek Žnidarič, M. Pompe Novak, U. Kuhar, P. Hostnik, F. Dattola, T. Carletti, A. Marcello, P. Kogovšek, Data for: In silico characterisation of a novel SARS-CoV-2 Envelope protein inhibitor and in vitro validation against Murine coronavirus, 2025, https://doi.org/10.5281/zenodo.17815979.
[42] I.F. De Castro, L. Volonté, C. Risco, Virus factories: biogenesis and structural design: biogenesis and architecture of virus factories, Cell. Microbiol. 15 (2013) 24–34, https://doi.org/10.1111/cmi.12029.
[43] S. Eymieux, Y. Rouillé, O. Terrier, K. Seron, E. Blanchard, M. Rosa-Calatrava, J. Dubuisson, S. Belouzard, P. Roingeard, Ultrastructural modifications induced by SARS-CoV-2 in Vero cells: a kinetic analysis of viral factory formation, viral particle morphogenesis and virion release, Cell. Mol. Life Sci. 78 (2021) 3565–3576, https://doi.org/10.1007/s00018-020-03745-y.
[44] Y. Cao, J. Wang, F. Jian, T. Xiao, W. Song, A. Yisimayi, W. Huang, Q. Li, P. Wang, R. An, J. Wang, Y. Wang, X. Niu, S. Yang, H. Liang, H. Sun, T. Li, Y. Yu, Q. Cui, S. Liu, X. Yang, S. Du, Z. Zhang, X. Hao, F. Shao, R. Jin, X. Wang, J. Xiao, Y. Wang, X.S. Xie, Omicron escapes the majority of existing SARS-CoV-2 neutralizing antibodies, Nature 602 (2022) 657–663, https://doi.org/10.1038/s41586-021-04385-3.
[45] S. Podder, A. Ghosh, T. Ghosh, Mutations in membrane-fusion subunit of spike glycoprotein play crucial role in the recent outbreak of COVID-19, J. Med. Virol. 93 (2021) 2790–2798, https://doi.org/10.1002/jmv.26598.
[46] S. Zhou, P. Lv, M. Li, Z. Chen, H. Xin, S. Reilly, X. Zhang, SARS-CoV-2 E protein: pathogenesis and potential therapeutic development, Biomed. Pharmacother. 159 (2023) 114242, https://doi.org/10.1016/j.biopha.2023.114242.
[47] T.L. Toft-Bertelsen, M.G. Jeppesen, E. Tzortzini, K. Xue, K. Giller, S. Becker, A. Mujezinovic, B.H. Bentzen, L.B. Andreas, A. Kolocouris, T.N. Kledal, M. M. Rosenkilde, Amantadine inhibits known and novel ion channels encoded by SARS-CoV-2 in vitro, Commun. Biol. 4 (2021) 1347, https://doi.org/10.1038/s42003-021-02866-9.
[48] R.A. Bright, M. Medina, X. Xu, G. Perez-Oronoz, T.R. Wallis, X.M. Davis, L. Povinelli, N.J. Cox, A.I. Klimov, Incidence of adamantane resistance among influenza A (H3N2) viruses isolated worldwide from 1994 to 2005: a cause for concern, Lancet 366 (2005) 1175–1181, https://doi.org/10.1016/S0140-6736(05)67338-2.
[49] J. Mancilla-Galindo, J.Ó. García-Méndez, J. Márquez-Sánchez, R.E. Reyes-Casarrubias, E. Aguirre-Aguilar, H.I. Rocha-González, A. Kammar-García, All-cause mortality among patients treated with repurposed antivirals and antibiotics for COVID-19 in Mexico City: a real-world observational study, EXCLI J. 20 (2021) Doc199, https://doi.org/10.17179/EXCLI2021-3413. ISSN 1611-2156.
[50] C. Verdiá-Báguena, J.L. Nieto-Torres, A. Alcaraz, M.L. DeDiego, J. Torres, V. M. Aguilella, L. Enjuanes, Coronavirus E protein forms ion channels with functionally and structurally-involved membrane lipids, Virology 432 (2012) 485–494, https://doi.org/10.1016/j.virol.2012.07.005.
[51] J. Torres, U. Maheswari, K. Parthasarathy, L. Ng, D.X. Liu, X. Gong, Conductance and amantadine binding of a pore formed by a lysine-flanked transmembrane domain of SARS coronavirus envelope protein, Protein Sci. 16 (2007) 2065–2071, https://doi.org/10.1110/ps.062730007.
[52] D. Schoeman, B.C. Fielding, Coronavirus envelope protein: current knowledge, Virol. J. 16 (2019) 69, https://doi.org/10.1186/s12985-019-1182-0.
[53] E. Steinmann, F. Penin, S. Kallis, A.H. Patel, R. Bartenschlager, T. Pietschmann, Hepatitis C virus p7 protein is crucial for assembly and release of infectious Virions, PLoS Pathog. 3 (2007) e103, https://doi.org/10.1371/journal.ppat.0030103.
[54] M.J. Sarmento, A. Llorente, T. Petan, D. Khnykin, I. Popa, M. Nikolac Perkovic, M. Konjevod, M. Jaganjac, The expanding organelle lipidomes: current knowledge and challenges, Cell. Mol. Life Sci. 80 (2023) 237, https://doi.org/10.1007/s00018-023-04889-3.
[55] Z. Zhao, Y. Xiao, L. Xu, Y. Liu, G. Jiang, W. Wang, B. Li, T. Zhu, Q. Tan, L. Tang, H. Zhou, X. Huang, H. Shan, Glycyrrhizic acid nanoparticles as antiviral and anti-inflammatory agents for COVID-19 treatment, ACS Appl. Mater. Interfaces 13 (2021) 20995–21006, https://doi.org/10.1021/acsami.1c02755.
[56] R. Burrer, B.W. Neuman, J.P.C. Ting, D.A. Stein, H.M. Moulton, P.L. Iversen, P. Kuhn, M.J. Buchmeier, Antiviral effects of antisense morpholino oligomers in murine coronavirus infection models, J. Virol. 81 (2007) 5637–5648, https://doi.org/10.1128/JVI.02360-06.
[57] Y. Zhou, K.A. Gammeltoft, A. Galli, A. Offersgaard, U. Fahnøe, S. Ramirez, J. Bukh, J.M. Gottwein, Efficacy of ion-channel inhibitors amantadine, memantine and rimantadine for the treatment of SARS-CoV-2 in vitro, Viruses 13 (2021) 2082, https://doi.org/10.3390/v13102082.
[58] S.H. Park, H. Siddiqi, D.V. Castro, A.A. De Angelis, A.L. Oom, C.A. Stoneham, M. K. Lewinski, A.E. Clark, B.A. Croker, A.F. Carlin, J. Guatelli, S.J. Opella, Interactions of SARS-CoV-2 envelope protein with amilorides correlate with antiviral activity, PLoS Pathog. 17 (2021) e1009519, https://doi.org/10.1371/journal.ppat.1009519.
[59] E.Y. Gong (Ed.), Antiviral Methods and Protocols, Humana Press, Totowa, NJ, 2013, https://doi.org/10.1007/978-1-62703-484-5.
[60] F. Chen, K.H. Chan, Y. Jiang, R.Y.T. Kao, H.T. Lu, K.W. Fan, V.C.C. Cheng, W.H. W. Tsui, I.F.N. Hung, T.S.W. Lee, In vitro susceptibility of 10 clinical isolates of SARS coronavirus to selected antiviral compounds, J. Clin. Virol. 31 (2004) 69–75, https://doi.org/10.1016/j.jcv.2004.03.003.
[61] U. Breitinger, N.S. Farag, N.K.M. Ali, M. Ahmed, M.A. El-Azizi, H.-G. Breitinger, Cell viability assay as a tool to study activity and inhibition of hepatitis C p7 channels, J. Gen. Virol. 102 (2021), https://doi.org/10.1099/jgv.0.001571.
[62] S. Griffin, C. StGelais, A.M. Owsianka, A.H. Patel, D. Rowlands, M. Harris, Genotype-dependent sensitivity of hepatitis C virus to inhibitors of the p7 ion channel, Hepatology 48 (2008) 1779–1790, https://doi.org/10.1002/hep.22555.
[63] M.L. DeDiego, E. Álvarez, F. Almazán, M.T. Rejas, E. Lamirande, A. Roberts, W.-J. Shieh, S.R. Zaki, K. Subbarao, L. Enjuanes, A severe acute respiratory syndrome coronavirus that lacks the E gene is attenuated in vitro and in vivo, J. Virol. 81 (2007) 1701–1713, https://doi.org/10.1128/JVI.01467-06.
[64] J.M. Jimenez-Guardeño, J.L. Nieto-Torres, M.L. DeDiego, J.A. Regla-Nava, R. Fernandez-Delgado, C. Castaño-Rodriguez, L. Enjuanes, The PDZ-binding motif of severe acute respiratory syndrome coronavirus envelope protein is a determinant of viral pathogenesis, PLoS Pathog. 10 (2014) e1004320, https://doi.org/10.1371/journal.ppat.1004320.
[65] F. Alvarez, G.D. De Melo, F. Larrous, L. Kergoat, B. Boëda, V. Michel, D. Seilhean, M. Tichit, D. Hing, D. Hardy, E. Kornobis, H. Bourhy, N. Wolff, C. Caillet-Saguy, The SARS-CoV-2 envelope PDZ binding motif acts as a virulence factor disrupting host's epithelial cell–cell junctions, Cell. Mol. Biol. Lett. 30 (2025) 80, https://doi.org/10.1186/s11658-025-00758-y.
[66] J. Ortego, J.E. Ceriani, C. Patiño, J. Plana, L. Enjuanes, Absence of E protein arrests transmissible gastroenteritis coronavirus maturation in the secretory pathway, Virology 368 (2007) 296–308, https://doi.org/10.1016/j.virol.2007.05.032.
[67] K. Miura, Y. Suzuki, K. Ishida, M. Arakawa, H. Wu, Y. Fujioka, A. Emi, K. Maeda, R. Hamajima, T. Nakano, T. Tenno, H. Hiroaki, E. Morita, Distinct motifs in the E protein are required for SARS-CoV-2 virus particle formation and lysosomal deacidification in host cells, J. Virol. 97 (2023) e00426–23, https://doi.org/10.1128/jvi.00426-23.
[68] G.J. Pearson, H.V. Mears, M. Broncel, A.P. Snijders, D.L.V. Bauer, J.G. Carlton, ER-export and ARFRP1/AP-1–dependent delivery of SARS-CoV-2 envelope to lysosomes controls late stages of viral replication, Sci. Adv. 10 (2024) eadl5012, https://doi.org/10.1126/sciadv.adl5012.
[69] W.-A. Wang, A. Carreras-Sureda, N. Demaurex, SARS-CoV-2 infection alkalinizes the ERGIC and lysosomes through the viroporin activity of the viral envelope protein, J. Cell Sci. 136 (2023) jcs260685, https://doi.org/10.1242/jcs.260685.

[70] S. Ghosh, T.A. Dellibovi-Ragheb, A. Kerviel, E. Pak, Q. Qiu, M. Fisher, P. M. Takvorian, C. Bleck, V.W. Hsu, A.R. Fehr, S. Perlman, S.R. Achar, M.R. Straus, G.R. Whittaker, C.A.M. De Haan, J. Kehrl, G. Altan-Bonnet, N. Altan-Bonnet, B-Coronaviruses use lysosomes for egress instead of the biosynthetic secretory pathway, Cell 183 (2020) 1520–1535.e14, https://doi.org/10.1016/j.cell.2020.10.039.

[71] P. Baudoux, C. Carrat, L. Besnardeau, B. Charley, H. Laude, Coronavirus Pseudoparticles formed with recombinant M and E proteins induce alpha interferon synthesis by leukocytes, J. Virol. 72 (1998) 8636–8643, https://doi.org/10.1128/JVI.72.11.8636-8643.1998.

[72] J. Maeda, A. Maeda, S. Makino, Release of coronavirus E protein in membrane vesicles from virus-infected cells and E protein-expressing cells, Virology 263 (1999) 265–272, https://doi.org/10.1006/viro.1999.9955.

[73] E. Corse, C.E. Machamer, Infectious bronchitis virus E protein is targeted to the Golgi complex and directs release of virus-like particles, J. Virol. 74 (2000) 4319–4326, https://doi.org/10.1128/JVI.74.9.4319-4326.2000.

[74] A. Zumla, J.F.W. Chan, E.I. Azhar, D.S.C. Hui, K.-Y. Yuen, Coronaviruses — drug discovery and therapeutic options, Nat. Rev. Drug Discov. 15 (2016) 327–347, https://doi.org/10.1038/nrd.2015.37.

[75] M. Merad, J.C. Martin, Pathological inflammation in patients with COVID-19: a key role for monocytes and macrophages, Nat. Rev. Immunol. 20 (2020) 355–362, https://doi.org/10.1038/s41577-020-0331-4.

[76] D. Forni, R. Cagliani, M. Clerici, M. Sironi, Molecular evolution of human coronavirus genomes, Trends Microbiol. 25 (2017) 35–48, https://doi.org/10.1016/j.tim.2016.09.001.